# Square lattice photonic crystal surface mode lasers

**Tsan-Wen Lu,* Shao-Ping Lu, Li-Hsun Chiu, and Po-Tsung Lee**

*Department of Photonics and Institute of Electro-Optical Engineering, National Chiao Tung University Rm. 415, CPT Building, 1001 Ta Hsueh Road, Hsinchu 30010, Taiwan*
**ricky.eo94g@nctu.edu.tw*

**Abstract:** In this report, we propose a square lattice photonic crystal hetero-slab-edge microcavity design. In numerical simulations, three surface modes in this microcavity are investigated and optimized by tuning the slab-edge termination $\tau$ and gradual mirror layer. High simulated quality ($Q$) factor of $2.3 \times 10^5$ and small mode volume of 0.105 $\mu m^3$ are obtained from microcavity with $\tau = 0.80$. In experiments, we obtain and identify different surface modes lasing. The surface mode in the second photonic band gap shows a very-low threshold of 140 μW and high $Q$ factor of 5,500, which could be an avenue to low-threshold optical lasers and highly sensitive sensor applications with efficient light-matter interactions.



**OCIS codes:** (230.5298) Photonic crystals; (140.3945) Microcavities; (140.5960) Semiconductor lasers.

## References and links

1. P. Yeh, *Optical Waves in Layered Media*, (Wiley, New York, 2005).
2. R. D. Meade, K. D. Brommer, A. M. Rappe, and J. D. Joannopoulos, "Electromagnetic Bloch waves at the surface of a photonic crystal," Phys. Rev. B Condens. Matter **44**(19), 10961–10964 (1991).
3. W. M. Robertson, G. Arjavalingam, R. D. Meade, K. D. Brommer, A. M. Rappe, and J. D. Joannopoulos, "Observation of surface photons on periodic dielectric arrays," Opt. Lett. **18**(7), 528–530 (1993).
4. K. Ishizaki, and S. Noda, "Manipulation of photons at the surface of three-dimensional photonic crystals," Nature **460**(7253), 367–370 (2009).
5. W. Śmigaj, "Model of light collimation by photonic crystal surface modes," Phys. Rev. B **75**(20), 205430 (2007).
6. H. Caglayan, I. Bulu, and E. Ozbay, "Off-axis directional beaming via photonic crystal surface modes," Appl. Phys. Lett. **92**(9), 092114 (2008).
7. H. C. Chen, K. K. Tsia, and A. W. Poon, "Surface modes in two-dimensional photonic crystal slabs with a flat dielectric margin," Opt. Express **14**(16), 7368–7377 (2006).
8. Yu. A. Vlasov, N. Moll, and S. J. McNab, "Mode mixing in asymmetric double-trench photonic crystal waveguides," J. Appl. Phys. **95**(9), 4538–4544 (2004).
9. V. S. Volkov, S. I. Bozhevolnyi, L. H. Frandsen, and M. Kristensen, "Direct observation of surface mode excitation and slow light coupling in photonic crystal waveguides," Nano Lett. **7**(8), 2341–2345 (2007).
10. S. Xiao, and M. Qiu, "Optical microcavities based on surface modes in two-dimensional photonic crystals and silicon-on-insulator photonic crystals," J. Opt. Soc. Am. B **24**(5), 1225–1229 (2007).
11. Z. Zhang, M. Dainese, L. Wosinski, S. Xiao, M. Qiu, M. Swillo, and U. Andersson, "Optical filter based on two-dimensional photonic crystal surface-mode cavity in amorphous silicon-on-silica structure," Appl. Phys. Lett. **90**(4), 041108 (2007).
12. J. Wang, Y. Song, W. Yan, and M. Qiu, "High-Q photonic crystal surface-mode cavities on crystalline SOI structures," Opt. Commun. **283**(11), 2461–2464 (2010).
13. J. K. Yang, S. H. Kim, G. H. Kim, H. G. Park, Y. H. Lee, and S. B. Kim, "Slab-edge modes in two-dimensional photonic crystals," Appl. Phys. Lett. **84**(16), 3016–3018 (2004).
14. T. W. Lu, Y. H. Hsiao, W. D. Ho, and P. T. Lee, "Photonic crystal hetero-slab-edge microcavity with high quality factor surface mode for index sensing," Appl. Phys. Lett. **94**(14), 141110 (2009).
15. V. N. Konopsky, and E. V. Alieva, "A biosensor based on photonic crystal surface waves with an independent registration of the liquid refractive index," Biosens. Bioelectron. **25**(5), 1212–1216 (2010).
16. T. W. Lu, Y. H. Hsiao, W. D. Ho, and P. T. Lee, "High-index sensitivity of surface mode in photonic crystal hetero-slab-edge microcavity," Opt. Lett. **35**(9), 1452–1454 (2010).
17. Y. Tanaka, T. Asano, and S. Noda, "Design of Photonic Crystal Nanocavity with Q-factor of ~$10^9$," J. Lightwave Technol. **26**(11), 1532–1539 (2008).
18. J. D. Joannopoulos, R. D. Meade, and J. N. Winn, *Photonic Crystals: Molding the Flow of Light*, (Princeton Univ. Press, 2008).

#135180 - $15.00 USD Received 15 Sep 2010; revised 27 Oct 2010; accepted 22 Nov 2010; published 2 Dec 2010

19. S. H. Kim, S. K. Kim, and Y. H. Lee, "Vertical beaming of wavelength-scale photonic crystal resonators," Phys. Rev. B **73**(23), 235117 (2006).

## 1. Introduction

The surface waves exist at the surfaces of dielectric photonic crystals (*PhCs*) via the confinements of total-internal reflection (*TIR*) and photonic band-gap (*PBG*) effects, which have been theoretically and experimentally investigated in one- [1], two- (*2D*) [2], and three-dimensional (*3D*) [3,4] *PhCs*. Unlike the surface plasmonic wave in metallic surface, it is almost absorption-free for surface wave in dielectric *PhC* surface, which could provide efficient light-matter interactions for various optical devices. Recently, based on this surface wave, *2D PhC* planar waveguides with directional emissions [5,6] and efficient coupling [7–9] have been studied and demonstrated, which would be the key components in constructing versatile planar photonic circuits. Moreover, *PhC* microcavities with confined surface waves [10–14] also attract lots of attentions owing to well-confining the photon flow in a very condensed volume at the dielectric surface, which can be applied to optical filters [11,12], lasers [4,13,14], sensors [15,16], and so on. Because the surface mode extends more field into the environment at the surface than general defect modes confined inside the *PhC* micro- and nano-cavities, it can provide strong interactions with the environmental analyte and is beneficial for highly sensitive optical sensing of protein binding [15], index variation [16] and so on. Although the surface mode tends to extend out of the cavity, high quality (*Q*) factor can be still achieved by proper cavity designs for *2D* [14] and *3D* [4] PhC low-threshold laser candidates. For example, in our previous work [14], we have initially proposed a mode gap effect to confine surface wave in a finite triangular-*PhC* slab-edge segment and demonstrated the surface mode lasing actions. However, the thorough investigations on surface modes in different slab-edge facets and precisely-controlled fabrication process for realizing the optimized slab-edge design have not been done.

In this report, even though the square-*PhC* has weaker *PBG* effect than that of the triangular-*PhC*, we show that high *Q* surface modes can be created in a square-*PhC* slab-edge based on our proposed mode gap confinement mechanism, which has not been studied and demonstrated yet. We investigate and optimize different surface modes in square-*PhC* slab-edge microcavities with reduced cavity sizes and different facets $\tau$ in simulations, which provides a guideline for achieving high *Q* and low threshold surface modes lasing.

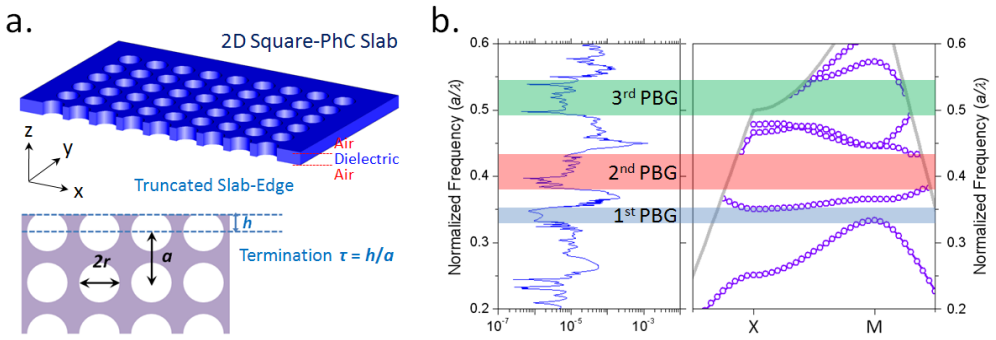


Fig. 1. (a) (top) Scheme of *2D* truncated square-*PhC* slab and (bottom) the definition of slab-edge termination parameter $\tau$. (b) The simulated *TE*-like band diagram (right) and transmission spectrum (left) of *2D* square-*PhC* slab by *3D PWE* and *FDTD* methods.

In experiments, we optimize the fabrication process by proximity correction for electron-beam lithography, which enables us to precisely obtain the desired parameters of the slab-edge microcavities. In measurements, high *Q* and low threshold surface modes lasing actions at different slab-edge terminations are obtained and identified.

#135180 - $15.00 USD Received 15 Sep 2010; revised 27 Oct 2010; accepted 22 Nov 2010; published 2 Dec 2010

## 2. Surface modes in square-PhC microcavity

For a *2D* square-*PhC* dielectric slab with air cladding shown in Fig. 1(a), the air hole radius ($r$) over lattice constant ($a$) ($r/a$) ratio, slab thickness, and refractive index are set to be 0.38, 220 nm, and 3.4, respectively. The simulated transverse-electric-like (*TE*-like) band diagram of square-*PhC* dielectric slab by *3D* plane-wave expansion (*PWE*) method is shown in Fig. 1(b). The *1st-PBG* is ranged from 0.33 to 0.36 in normalized frequency ($a/\lambda$), which is confirmed by *3D* finite-difference time-domain (*FDTD*) simulated transmission spectrum also shown in Fig. 1(b). The *1st-PBG* corresponds to a spectral width of 100 nm when $a$ = 500 nm, which could not provide sufficient confinement for surface modes at certain slab-edge terminations. Thus, besides the *1st-PBG*, in our following design, we will also use the *2nd-PBG* with larger spectral width from 0.38 to 0.43, as shown in Fig. 1(b).

The surface wave can exist at the *2D* truncated *PhC* slab-edge shown in Fig. 1(a) by the *PBG* and *TIR* confinements. To well confine the surface wave in a slab-edge segment with finite length, we had designed a hetero-slab-edge (*HSE*) interface with mode gap effect. For a given square-*PhC* slab-edge $\tau_C$ shown in Fig. 2(a), we can obtain a slab-edge $\tau_C$' with decreased surface mode frequency by shrinking and shifting the air holes at the slab-edge, as shown in Fig. 2(a). The $r/a$ ratio difference between the slab-edges $\tau_C$ and $\tau_C$' is defined as $\Delta r/a$. The simulated surface mode dispersion curves under different $\Delta r/a$ are shown in Fig. 2(b). For the decreased surface mode frequency of slab-edge $\tau_C$', a mode gap represented by the shadow region in Fig. 2(b) will form owing to the surface mode frequency difference between the slab-edges $\tau_C$ and $\tau_C$'. In the slab-edge $\tau_C$, the surface mode with frequency inside the mode gap is forbidden to propagate in slab-edge $\tau_C$'. Thus, we can use the slab-edge $\tau_C$' as a mirror layer for slab-edge $\tau_C$ to form a microcavity, as shown in Fig. 2(c). To reduce the scattering loss between the cavity $\tau_C$ and the outer mirror region $\tau_C$' [17], we design a gradual mirror region $\tau_G$, where the air-hole $r/a$ ratio at slab-edge is linearly changed, as shown in Fig. 2(c). The initial parameters are as follows: (1) The $r/a$ ratio and length of the cavity $\tau_C$ are 0.38 and 6$a$. (2) The $\Delta r/a$ ratio is chosen as 0.03. (3) The length of gradual mirror $\tau_G$ is 5$a$.

According to above parameters, we vary the slab-edge termination parameter $\tau$ (as defined in Fig. 1(a)) of cavity $\tau_C$ from 0 to 0.90. By *3D FDTD* simulations, we find three high $Q$ surface modes under different $\tau$, which are denoted as the $DD_1$-, $DD_2$-, and $DD_3$- modes. The surface modes we investigate here are all *0th*-order fundamental modes. The first and second

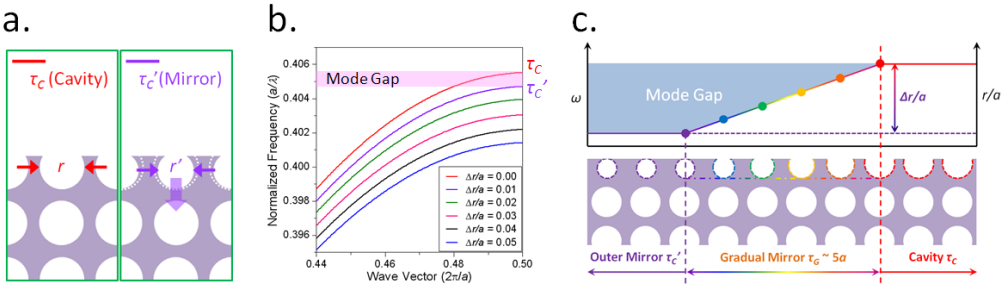


Fig. 2. (a) Scheme of square-*PhC* slab-edges $\tau_C$ and $\tau_C$'. The air holes at slab-edge $\tau_C$' are shifted and shrunk, which leads to the decreased frequency of surface mode and a mode gap region denoted by the shadow region in (b) is formed. (b) The surface mode dispersion curves under different $\Delta r/a$. The $r/a$ ratio difference between slab-edges $\tau_C$ and $\tau_C$' is defined as $\Delta r/a$. (c) Scheme of square-*PhC HSE* interface that forms mirror layers, including the outer mirror $\tau_C$' and gradual mirror $\tau_G$, while the slab-edge $\tau_C$ is served as the cavity region.

#135180 - $15.00 USD Received 15 Sep 2010; revised 27 Oct 2010; accepted 22 Nov 2010; published 2 Dec 2010

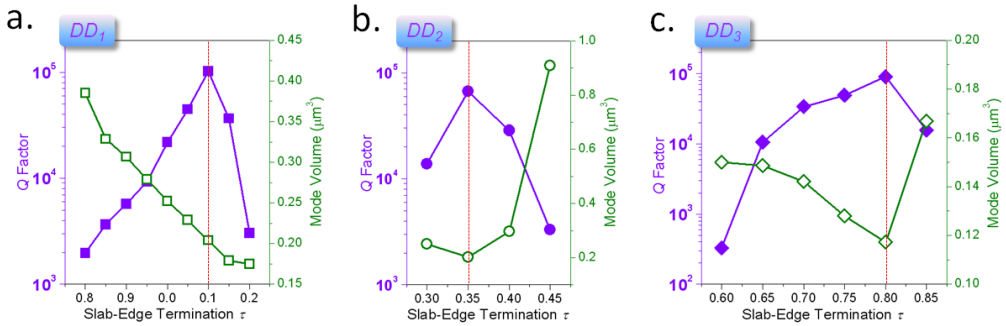


Fig. 3. The simulated $Q$ factors and mode volumes of the *0th*-order (a) $DD_1$-, (b) $DD_2$-, and (c) $DD_3$-modes under different $\tau$. The $\Delta r/a$ is fixed at 0.03.

letters stand for the mode behaviors in the air and PhC regions, respectively. We use the letters *D* and *E* to mean *Decay* and *Extended* [18]. The simulated $Q$ factors and mode volumes ($V$) of the three surface modes under different $\tau$ are shown in Figs. 3(a)–3(c). The $DD_1$- and $DD_3$-modes both lie inside the *2nd-PBG* and high $Q$ factors of $1.0 \times 10^5$ and $9.1 \times 10^4$ can be obtained when $\tau$ = 0.10 and 0.80, respectively. However, we find the mode volume of the $DD_3$-mode (~0.117 μm$^3$) is smaller than that of the $DD_1$-mode (~0.204 μm$^3$), which shows a higher $Q/V$ value of $DD_3$-mode and is beneficial for laser source in quantum electron dynamic devices and photonic integrated circuits. Thus, in the following experiments, we will focus on the $DD_3$-mode. At $\tau$ = 0.80, we optimize the $Q$ factor of the $DD_3$-mode in *HSE* microcavity by varying $\Delta r/a$ from 0.02 to 0.18. The simulated $Q$ factors and mode volumes under different $\Delta r/a$ are shown in Fig. 4(a). When $\Delta r/a$ = 0.09, we obtain a high $Q$ factor of $2.3 \times 10^5$ and a small $V$ of 0.105 μm$^3$ (close to one wavelength cubic). It is worthy to note the surface mode volume is very small even the cavity size is quite large (6*a*), which originates from its feature of highly concentrated field at the surface. The simulated electric field components ($E_x$ and $E_y$) of the $DD_3$-mode are shown in Fig. 4(b). We can observe that the electric field concentrates at the surface of the microcavity region and very small field fraction extends into the square-*PhC*, which reveals good confinement by the *2nd-PBG* effect. In addition, in Fig. 4(b), the $E_x$- and $E_y$-fields are even and odd symmetric to the *y*-axis (dash line in Fig. 4(b)), respectively. That means the $E_y$ far-field will be cancelled and implies the $E_x$ far-field emission contributes more to the emissions inside the collectable radiation angle [19], for example, ± 30°, when the emission is collected by an objective lens with numerical aperture of 0.5.

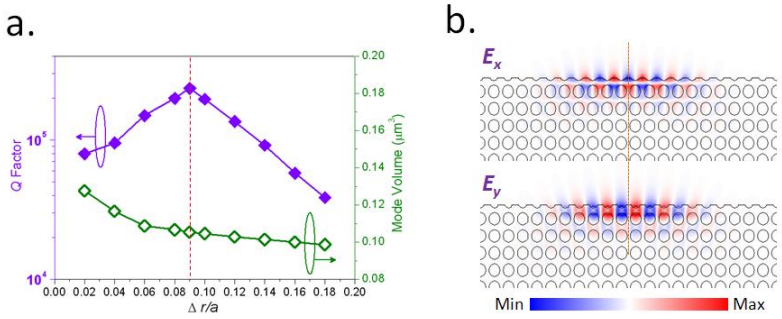


Fig. 4. (a) The simulated $Q$ factor and mode volume of the $DD_3$-mode under fixed $\tau$ of 0.80 and different $\Delta r/a$ from 0.02 to 0.18. High $Q$ factor and small mode volume of $2.3 \times 10^5$ and 0.105 μm$^3$ are obtained when $\Delta r/a$ = 0.09. (b) The simulated $E_x$- and $E_y$-fields of the $DD_3$-mode in microcavity with $\tau$ = 0.80 and $\Delta r/a$ = 0.09, which are even and odd symmetric to the *y*-axis (dash line).

#135180 - $15.00 USD Received 15 Sep 2010; revised 27 Oct 2010; accepted 22 Nov 2010; published 2 Dec 2010

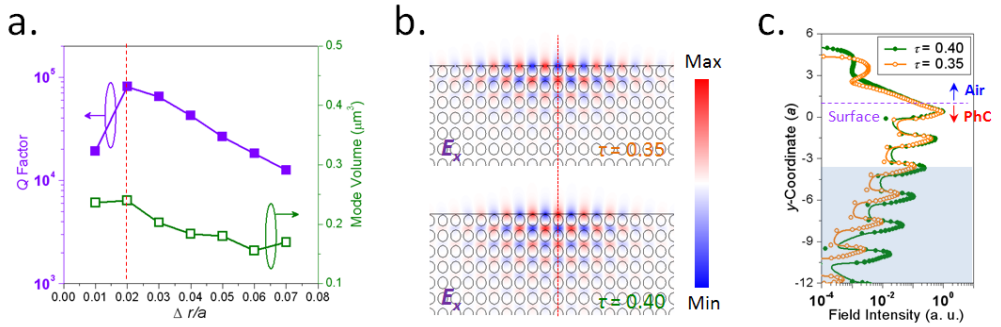


Fig. 5. (a) The simulated $Q$ factor and mode volume of the $DD_2$-mode under fixed $\tau$ of 0.35 and different $\Delta r/a$ from 0.01 to 0.07. (b) The simulated $E_x$-fields of the $DD_2$-mode in microcavities with $\tau$ = 0.35 (top) and 0.40 (bottom) and (c) their $E_x$-field distributions along the dash line in (b).

Furthermore, the $DD_2$-mode inside the *1st-PBG* reaches its highest $Q$ factor of $6.4 \times 10^4$ and smallest mode volume of 0.203 $\mu m^3$ at $\tau$ = 0.35. We then optimize the $DD_2$-mode by varying $\Delta r/a$ from 0.01 to 0.07 at $\tau$ = 0.35. The simulated $Q$ factors and mode volumes under different $\Delta r/a$ are shown in Fig. 5(a). When $\Delta r/a$ = 0.02, we obtain a high $Q$ factor of $8.0 \times 10^4$ and the simulated $E_x$-field distribution is shown in Fig. 5(b), where we can observe the $E_x$-field extends more into the square-*PhC* than that of the $DD_3$-mode shown in Fig. 4(b). This is caused by the insufficient *1st-PBG* confinement, which makes the $DD_2$-mode become a *DE*-like mode. This could be responsible for its lower $Q$ factor and larger mode volume than those of the $DD_3$-mode. This phenomenon becomes more significant when $\tau$ increases to be 0.40 or decreases to be 0.30, where the $Q$ factor appreciably decreases and the mode volume increases, respectively, as shown in Fig. 3(b). The simulated $E_x$-field of the $DD_2$-mode in microcavity with $\tau$ = 0.40 is also shown in Fig. 5(b). The $E_x$-field distributions of the $DD_2$-mode in microcavities with $\tau$ = 0.35 and 0.40 along the dash line shown in Fig. 5(b) are shown in Fig. 5(c). Clearly, the $E_x$-field of the $DD_2$-mode at $\tau$ = 0.40 extends more into the square-*PhC* region, as shown by the shadow region in Fig. 5(c).

Thus, comparing the $DD_2$-mode with the $DD_3$-mode, we can conclude the *2nd*-PBG of square-*PhC* can provide more efficient confinement than the *1st-PBG*, which leads to high $Q$ factor and small mode volume of surface mode.

### 3. Surface modes lasing actions

In fabrication, the epitaxial structure consisted of four 10 nm compressively strained InGaAsP multi-quantum-wells (*MQWs*) with 220 nm thickness is prepared. The measured photoluminescence (*PL*) centered at 1530 nm is shown in Fig. 6(a). The *MQWs* is deposited a silicon nitride hard mask and spin-coated electron-beam resist in sequence. The square-*PhC* patterns are defined by electron-beam lithography on the resist layer. After a series of reactive ion etching and inductively coupled plasma etching, the square-*PhC* slab is formed by HCl selective wet-etching process. Designing the patterns with proper proximity corrections for electron-beam lithography is very important, which assures that we can fabricate the optimized $\tau$ and $\Delta r/a$ ratio obtained in simulation, and keep the $r/a$ ratio uniform near the slab-edge of the fabricated devices. Scanning electron microscope (*SEM*) pictures of the fabricated slab-edges with $\tau$ = 0 to 0.90 are shown in Fig. 6(b). However, there would be very slight $r/a$ ratio difference between the *PhC* patterns near and far away from the slab-edge. Top- and tilted-view *SEM* pictures of the square-*PhC HSE* microcavity are shown in Figs. 6(c) and 6(d). From the zoom-in *SEM* pictures of cavity $\tau_C$, gradual mirror $\tau_G$, and outer mirror $\tau_C'$ shown in Fig. 6(e), the fabricated $a$, $\tau$, $r/a$ and $\Delta r/a$ ratios are estimated to be 520 nm, 0.40, 0.38, and 0.02, respectively.

#135180 - $15.00 USD Received 15 Sep 2010; revised 27 Oct 2010; accepted 22 Nov 2010; published 2 Dec 2010

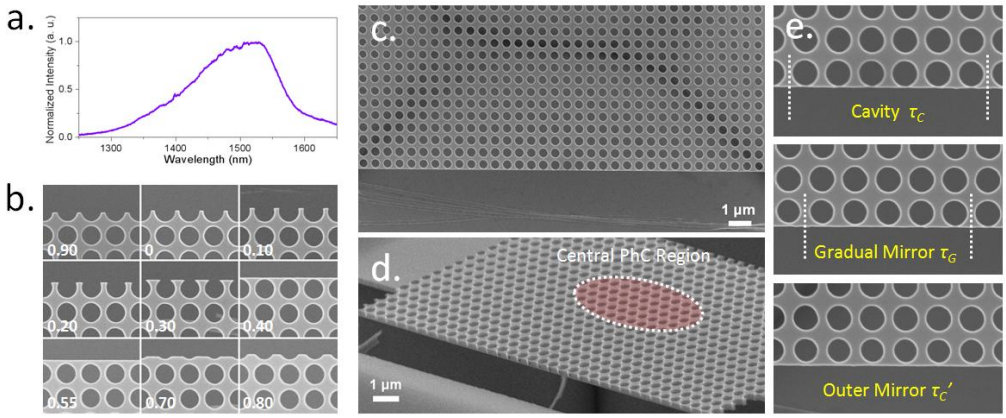


Fig. 6. (a) The measured *PL* spectrum of the InGaAsP *MQWs*. (b) *SEM* pictures of the fabricated slab-edges with different $\tau$ from 0 to 0.90. (c) Top- and (d) tilted-view *SEM* pictures of the square-*PhC HSE* microcavity with $\tau$ = 0.40. (e) The zoom-in *SEM* pictures of cavity $\tau_C$, gradual mirror $\tau_G$, and outer mirror $\tau_C'$, which show the well-controlled $\Delta r/a$ of 0.02.

According to the optimized results in simulation, the square-*PhC HSE* microcavity with fabricated $a$ = 620 nm, $r/a$ = 0.38, $\Delta r/a$ = 0.09, and $\tau$ = 0.80 shown as the insets in Fig. 7(a) is optically pumped by 20 ns pulse with 0.6% duty cycle at room temperature. The measured light-in light-out (*L-L*) curve and lasing spectrum in dB scale at 1556 nm are shown in Figs. 7(a) and 7(b), which show a very low threshold of 140 μW and side-mode suppression-ratio larger than 25 dB. The spectrum at 0.7 times threshold shown as the inset of Fig. 7(b) shows the measured line-width of 0.28 nm, which corresponds to a high estimated *Q* factor of 5,500. The localization property of surface mode in *HSE* microcavity can be easily confirmed by moving the excitation laser spot from microcavity to square-*PhC* and outer mirror regions, respectively, and no lasing action is observed when pumping these regions. To further confirm the surface mode lasing, lasing spectra of the $DD_3$-mode at different $\tau$ from 0.70 to 0.85 are obtained and shown in the top of Fig. 7(c). The measured normalized frequencies agree with the *3D FDTD* simulated results, as shown in the bottom of Fig. 7(c).

We also measure the *HSE* microcavity with fabricated $a$ = 520 nm, $r/a$ = 0.38, $\Delta r/a$ = 0.02, and $\tau$ = 0.35, shown as the inset of Fig. 8(a). From the measured spectrum in the top of Fig. 8(a), we observe three lasing peaks at 1480, 1505, and 1576 nm. The first two peaks are

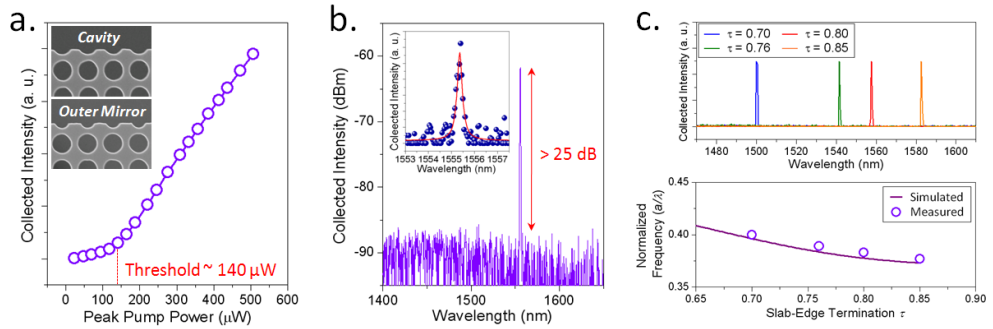


Fig. 7. (a) *L-L* curve and (b) lasing spectrum in dB scale of the $DD_3$-mode from microcavity with $\tau$ = 0.80 and $\Delta r/a$ = 0.09. The zoom-in *SEM* pictures of the measured microcavity and the spectrum below threshold are shown as the insets of (a) and (b). (c) Lasing wavelengths of the $DD_3$-mode under different $\tau$ from 0.70 to 0.85 (top), which agree with *3D FDTD* simulation results (bottom) quite well.

#135180 - $15.00 USD Received 15 Sep 2010; revised 27 Oct 2010; accepted 22 Nov 2010; published 2 Dec 2010

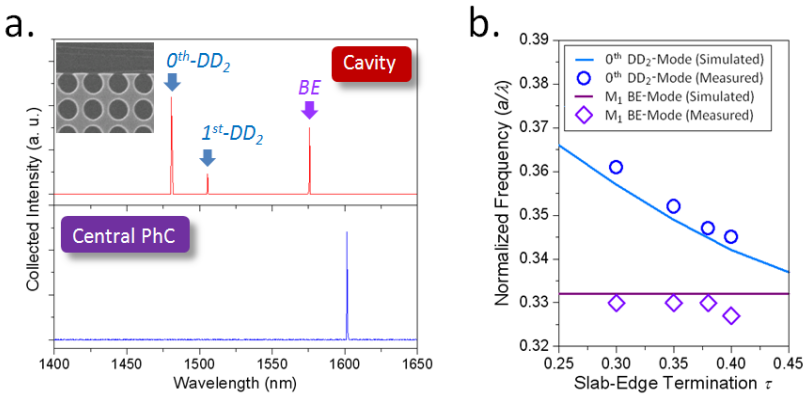


Fig. 8. (a) The measured lasing spectra from the *HSE* microcavity with $\tau$ = 0.35 when pumping (top) the cavity and (bottom) the central square-*PhC* regions. Lasing actions of the *0th*-, *1st*-order $DD_2$-modes and *BE*-mode can be observed when pumping the cavity, while only *BE*-mode lasing can be observed when pumping the central square-*PhC*. The zoom-in *SEM* picture of the measured *HSE* microcavity with $\tau$ = 0.35 is also shown as inset. (b) Comparisons between the *3D FDTD* simulated and measured frequencies of the *0th*-order $DD_2$- and *BE*-modes.

identified as *0th*- and *1st*-order $DD_2$-modes, by comparing with *3D FDTD* simulation results. The *0th*-order $DD_2$-mode is the mode we discuss and optimize in Fig. 3(b). Furthermore, we believe the lasing peak at 1576 nm comes from the band-edge (*BE*) mode at *M*-point of the *1st*-band ($M_1$). When the excitation laser spot is moved to the central square-*PhC* region denoted in Fig. 6(d), this peak can still be obtained while there is no $DD_2$-mode lasing observed, as shown in the bottom of Fig. 8(a) under 5 times the pump power used to obtain the top lasing spectrum of Fig. 8(a). This shows the field localization and extension features of the $DD_2$- and *BE*-modes, respectively. This also implies the *PhC* slab-edge presented here could efficiently lead out the emission of the *BE* slab modes confined inside the *PhC* slab. The wavelength shift of the *BE*-mode in Fig. 8(a) is attributed to the slightly shrunk *r/a* ratio of central square-*PhC* because of the proximity effect during electron-beam lithography. Moreover, the *BE*-mode can be further confirmed by its almost-constant frequency when $\tau$ is varied from 0.30 to 0.40, as shown in Fig. 8(b). In contrast, the *0th*-order $DD_2$-mode frequency decreases with increased $\tau$ from 0.30 to 0.40. Both of them agree with the *3D FDTD* simulated results shown in Fig. 8(b). Thus, we can confirm the lasing modes come from the $DD_2$- and *BE*-modes, respectively.

## 4. Summary

In this report, we propose a square-*PhC HSE* microcavity, which sustains different surface modes at different slab-edge terminations $\tau$. Via *3D FDTD* simulation, three different surface modes are investigated, including the $DD_1$- ($\tau$ = 0.80 - 0.20) and $DD_3$-modes ($\tau$ = 0.60 - 0.85) in the *2nd*-PBG, and the $DD_2$-mode ($\tau$ = 0.30 - 0.45) in the *1st-PBG*. By optimizing $\tau$ and gradual-mirror parameter $\Delta r/a$, we obtain a high *Q* factor of $2.3 \times 10^5$ and small mode volume of 0.105 $\mu m^3$ from the $DD_3$-mode at $\tau$ = 0.80 and $\Delta r/a$ = 0.09. In experiments, via designed proximity corrections in electron-beam lithography, we can well-control the desired fabricated $\tau$, $\Delta r/a$ ratio, and keep the *r/a* ratio uniform near the slab-edge of the fabricated devices. We obtain the $DD_2$- and $DD_3$-mode lasing actions from the *HSE* microcavities with $\tau$ = 0.35 and 0.80. These two modes are identified by wavelength shifts under different $\tau$, which differentiates them from the *BE*-mode at $M_1$-point extracted by *PhC* slab-edge with invariant wavelength. The $DD_3$-mode lasing shows a very low threshold of 140 μW and high measured *Q* factor of 5,500. Due to the feature of surface mode field concentrated at surface, we believe this microcavity design with surface mode could be an avenue to low-threshold optical laser and highly sensitive optical sensor applications with efficient light-matter interactions.

#135180 - $15.00 USD Received 15 Sep 2010; revised 27 Oct 2010; accepted 22 Nov 2010; published 2 Dec 2010

**Acknowledgements**

This work is supported by Taiwan's National Science Council (NSC) under contract number NSC-98-2221-E-009-015-MY2. The authors would like to thank the help from Center for Nano Science and Technology (CNST) of National Chiao Tung University, Taiwan.

#135180 - $15.00 USD Received 15 Sep 2010; revised 27 Oct 2010; accepted 22 Nov 2010; published 2 Dec 2010